ADVANCED FUNCTIONAL MATERIALS
www.afm-journal.de

Tuning the Electronic and Electrochemical Properties of 3D Porous Laser-Induced Graphene by Electrochemically Induced Deposition of Polyoxovanadate Nanoclusters for Flexible Supercapacitors

*Nikhil Arya, Sirshendu Dinda, Thomas Diemant, Ke Wang, Maximilian Fichtner, and Montaha Anjass**

The advancement of microelectronic devices mandates the development of flexible energy storage systems to enable the fabrication of miniaturized and wearable electronics. Herein, a sustainable approach is demonstrated for tuning the electronic and electrochemical properties of hierarchically porous laser-induced graphene (LIG) substrates. The methodology entails the electrochemical deposition of polyoxovanadate nanoclusters ($K_5(CH_3CN)_3[V_{12}O_{32}Cl]$ (= $K_5\{V_{12}\}$)) onto the highly porous LIG matrix. The comprehensive characterization is integrated through micro-Raman spectroscopy and in-depth X-ray photoelectron spectroscopy to elucidate the deposition mechanism and electronic properties of the fabricated electrode. The results indicate a significant correlation between the orientation of the deposited clusters and the non-crystalline regions of the LIG structure. Additionally, the cluster deposition results in a reduction of grain boundary defects in the nano-graphite lattice of LIG. The optimized electrode exhibits enhanced areal capacitance (C_A) of 125 mF cm^{-2} at a current density of 0.1 mA cm^{-2}, representing a fivefold improvement compared to the undoped LIG substrate. Furthermore, as a proof of concept, a flexible solid-state symmetrical supercapacitor device, fabricated with a PVA-H_2SO_4 gel electrolyte, demonstrates an areal capacitance of 24.92 mF cm^{-2} at current density of 0.1 mA cm^{-2} and exhibits exceptional cycling stability, enduring up to 5000 consecutive galvanostatic charge-discharge cycles.

1. Introduction

The transition from fossil-fuel-based systems to carbon-neutral and sustainable energy storage systems requires affordable modern energy storage systems with high power density and extended life cycles. The growing demand for such next-generation energy storage systems arises from their promising functionality in various applications, such as portable electronic devices, electric vehicles, energy harvesting, etc.[1–5] As a consequence, considerable research focuses on high-performance electrochemical double-layer supercapacitors (EDLSCs) due to their high power density, enhanced electrochemical stability, and remarkable charge-discharge cycle performance.[6] The working principle of EDLSCs relies on the non-faradaic fast adsorption/desorption of the electrolyte ions between the electrolyte and the highly electron/ion conductive porous electrode material. Over the past decade, graphene-based electrode materials have emerged as an

N. Arya, K. Wang, M. Anjass
Institute of Inorganic Chemistry I
Ulm University
Albert-Einstein-Allee 11, 89081 Ulm, Germany
E-mail: montaha.anjass@uni-ulm.de

The ORCID identification number(s) for the author(s) of this article can be found under https://doi.org/10.1002/adfm.202410943

DOI: 10.1002/adfm.202410943

N. Arya, S. Dinda, T. Diemant, M. Fichtner, M. Anjass
Helmholtz Institute Ulm for Electrochemical Energy Storage (HIU)
Helmholtzstr. 11, 89081 Ulm, Germany

T. Diemant, M. Fichtner
Karlsruhe Institute of Technology (KIT)
Institute of Nanotechnology
P. O. Box 3640, 76021 Karlsruhe, Germany

M. Anjass
Department of Chemistry
University of Sharjah
27272 Sharjah, United Arab Emirates

ideal choice for EDLSC electrodes due to their large 3D nano/microstructure surface area, excellent electronic properties, and high mechanical stability.[6] However, the intrinsic structural modification and restacking of the active graphene layers in pristine graphene-based electrodes cause poor ion and electron transport within the electrode, resulting in low theoretical capacitance and limited energy density.[7] To address these limitations, several strategies such as oxidation, exfoliation, and heteroatom insertion into graphene materials have been reported in order to enhance the pseudo-capacitive performance of graphene-based electrodes.[8–11]

Recently, laser-induced graphene has been extensively used as a promising electrode precursor for flexible supercapacitors (SCs) due to its unique physiochemical properties, good electrical conductivity, highly porous micro/nanostructure, and favorable thermal and mechanical stability.[12–14] LIG is generated by irradiating polyimide (PI) with a laser at a wavelength of about 500 nm; the high-temperature treatment and spontaneous gas formation on the PI layer result in a 3D, highly porous micro/nanostructure.[15] This method facilitates large-scale fabrication of flexible graphene materials while preserving important graphene properties for various applications such as electrocatalysis, sensors, SCs, and microfluidics.[16–20] The success of LIG as a flexible electrode matrix for application in SCs and micro-SCs has been attributed to excellent electrolyte ion diffusion within the porous LIG surface.[21–23] The capacitive performance of a pristine LIG surface is limited to less than 10 mF cm^{-2} due to the large number of non-functionalized capacitive sites.[12,13,24] Alternatively, a huge specific surface area and substantial crystallite defects enable LIG to be easily modified by functionalization and heteroatom doping. Previous reports on structural modification via heteroatom doping with boron (B), phosphorus (P), and nitrogen (N) have demonstrated an enhancement of capacitive performance by up to threefold.[25–28]

In this study, we show an easy and effective method for enhancing the capacitive charge storage performance by embedding vanadium oxide nanoclusters on hierarchical porous LIG. These molecular metal oxide structures are known as polyoxometalates (POMs). POMs are anionic metal oxoclusters of highly valent early transition metals (often Mo, W, and V) that form by self-assembly in solution.[29] POMs, specifically polyoxovanadates (POVs), have garnered attention due to their promising electrochemical properties and unique multivalent characteristics.[30] Moreover, these POV structures have set a new benchmark for successful heterometallic functionalization, opening up a systematic route to the study of controlled structural and electrochemical tuning.[31,32] Recent studies have investigated the interaction between alkali cations and POVs and demonstrated the influence of these cations on structural stability and electrochemical properties.[33] Schimpf and co-workers illustrated this influence of the concentration of the charge-balancing cation (K^+) on the coordination of the polyoxotungstate phase using the Preyssler-type polyoxoanion cluster $[NaP_5W_{30}O_{110}]^{14-}$.[34] Similarly, the Dawson-type polyoxotungstate showed cation-controlled reversible storage of up to 18 electrons in solution.[35] However, the technological application of POMs remains challenging due to the lack of a clear method to transform soluble POM species into a solid substance and immobilize them on a functional substrate. Interestingly, the cluster immobilization by electrochemical deposition leads to continuous film growth on the substrate in a more controlled manner. Hwu and co-workers, for instance, recently showed the electrochemical crystal growth of decavanadate-based organic-inorganic hybrids.[36]

Our group has recently provided the first proof of concept for a reversible electrochemically deposited thin film of the potassium-bridged molecular vanadium oxide cluster ($K_5(CH_3CN)_3$ $[V_{12}O_{32}Cl]$ (= $K_5\{V_{12}\}$)) or K-POV on a conductive surface.[37] The reduction of $K_5\{V_{12}\}$ in excess K^+ ions leads to the reduction-induced growth of a potassium-enriched homogeneous POV film on the conductive surface. Furthermore, comprehensive electrochemical studies provided in-depth understanding of the physicochemical properties, structural tuning, and redox activity of the electrochemically deposited $K_5\{V_{12}\}$-based thin film. Herein, we expand our investigation on a highly porous LIG graphene nanostructure as substrate, reporting a facile electrochemical deposition route that enables the successive deposition of reduced $K_5\{V_{12}\}$. Detailed spectroscopic investigation reveals that the deposition of $K_5\{V_{12}\}$ on the LIG nanostructure occurs via physisorption. Nevertheless, the deposited reduced $K_5\{V_{12}\}$ species exhibit high redox activity, enhancing the number of pseudocapacitive active sites and promoting reversible redox reactions and rapid charge storage capacity on the modified LIG electrode surface. During electrodeposition, reduction-induced growth of a potassium-enriched $K_x\{V_{12}\}$ film on the conductive surface occurred, facilitating the formation of mixed-valent vanadium centers V^V/V^{IV}. This unique property of POVs to change their oxidation state and incorporate transition metal has been utilized in various electrocatalysis applications.[38,39] The deposition of reduced $K_5\{V_{12}\}$ on the LIG surface enhances the electrocatalytic properties of the electrode, leading to the formation of various complexes between the vanadium oxide and electrolyte anions on the modified electrode. These vanadium-based oxosulphato/hydroxysulphato complexes prevent the LIG graphene substrate from restacking and transforming into a decomposed amorphous, soot-like carbon structure during charge-discharge cycles. Consequently, the high redox activity of the LIG electrode is sustained, enhancing the specific charge storage capacity of these $K_5\{V_{12}\}$ modified electrodes.

2. Result and Discussion

The $K_5\{V_{12}\}$ nanoclusters, employed in this study, were synthesized through a self-assembly process of two hexagonal $\{V_6\}$ rings, as depicted in **Figure 1a**. The electrochemical deposition and complex supramolecular aggregation on the porous LIG surface were initiated upon dissolving the $K_5\{V_{12}\}$ in an alkali metal salt-based supporting electrolyte of potassium hexafluorophosphate (KPF_6). The presence of a strong electropositive cation, such as K^+, in the solvent enables controlled crosslinking with the vanadium oxide framework, resulting in a homogeneous settlement within the nanoporous graphene network.[40] This potential-controlled deposition of $K_5\{V_{12}\}$ illustrates the indispensability of strong electropositive alkali metal cations for stabilizing the reduced cluster, leading to the development of highly redox-active supramolecular cluster growth on any conductive surface.[37]

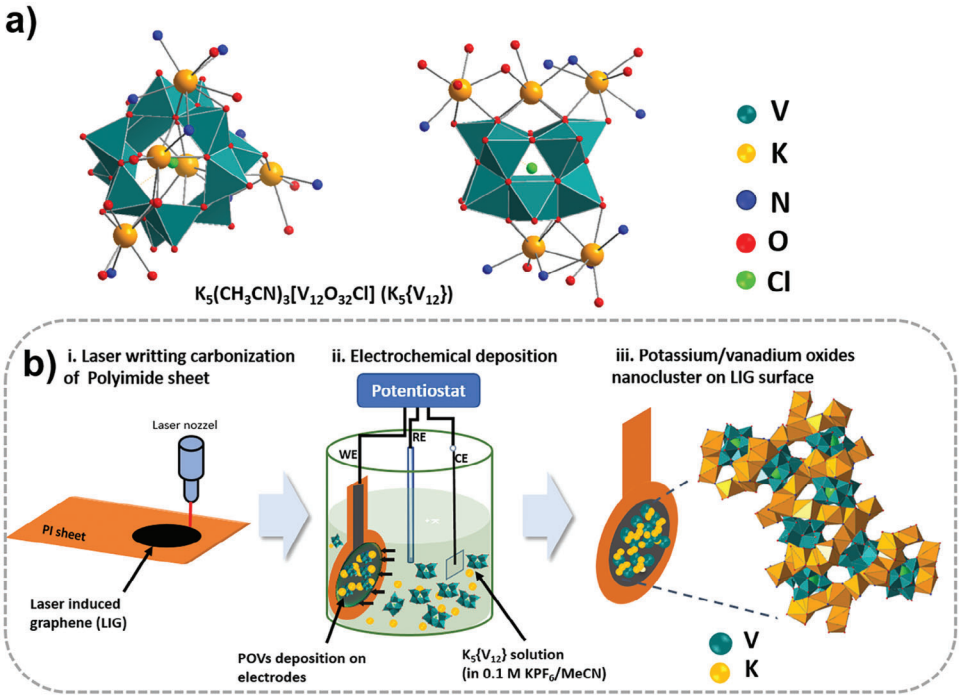

Figure 1. a) Molecular structure of the $K_5\{V_{12}\}$ cluster (left image: top view, right image: side view). b) Schematic representation of LIG electrode fabrication and electrochemical immobilization of $K_5\{V_{12}\}$. Color scheme: V (teal); O (red), N (blue), Cl (green), and K (yellow).

Figure 1b shows the main steps for preparing the K-POV/LIG electrodes. More experimental details can be found in the Supporting Information (SI). In brief, the LIG precursor was prepared by laser irradiating a polyimide sheet, generating an active area of 1 cm^2 for the deposition process.[12] The deposition of $K_5\{V_{12}\}$ was accomplished by cyclic voltammetry (CV) scans conducted within three different potential ranges: −250 – 250 mV, −500 – 500 mV, and −750 – 750 mV versus Ag^+/Ag, with the operating electrode scanned at 100 mV s^{-1} in a conventional three-electrode cell configuration using a non-aqueous ionic electrolyte solution (1 mM $K_5\{V_{12}\}$ in 0.1 M KPF_6 in MeCN). In each experiment, nine consecutive CV cycles were acquired (Figure S1a, Supporting Information). The modified LIG electrodes are labeled K-POV-250, K-POV-500, and K-POV−750 in the following, corresponding to the above-mentioned potential ranges.

To mitigate diffusion limitations during deposition, a 60-second rest period was introduced after every 3 consecutive CV cycles. The working electrode initially rested at 0 mV versus Ag^+/Ag, cycled toward the upper oxidative potential limit during the first sweep, and then reduced to the reduction potential limit. All the CVs that were measured showed a broad anodic peak at ≈220 mV versus Ag^+/Ag during the scan from the initial resting potential to the oxidative potential limit. This is in line with the solute $\{V_{12}\}$ cluster's characteristic reversible oxidation behavior.[37] Similarly, during the cathodic sweep to -500 mV versus Ag^+/Ag, a reduction process started at ≈100 mV versus Ag^+/Ag. This was caused by the partial reduction of the vanadium centers from V^{+V} to V^{+IV} oxidation state (Figure S1b, Supporting Information).[37] This reduction process facilitates stronger interaction between the reduced anionic cluster framework $\{V_{12}\}$ and dissolved K^+ ions, which enhanced the cluster's insolubility and resulted in the electrodeposition of the POVs on the LIG surface. Increasing the potential window from −500 to −750 mV versus Ag^+/Ag leads to an additional reduction feature in the CV at about −550 mV versus Ag^+/Ag, possibly representing a further reduction of the already deposited cluster species. This leads to an enhanced cathodic current observed for −750 mV versus Ag^+/Ag potential range. In addition, the following cycles observe a significant shift of the anodic peak (from 220 to 340 mV versus Ag^+/Ag), confirming that the charge compensating K^+ cations stabilized the reduced cluster, making its re-oxidation more difficult. These findings are in good agreement with a previous report.[37] The deposition of the cluster at a potential range of −750 to 750 mV versus Ag^+/Ag shows multiple redox peaks during the first CV cycle. This confirms that the $K_5\{V_{12}\}$ cluster has distinct redox-active properties in a higher potential range. To investigate the influence of the deposition of the $K_5\{V_{12}\}$ cluster on the LIG electrode, a blank CV measurement was performed on a fresh LIG electrode under similar conditions but without the $K_5\{V_{12}\}$ in the supporting electrolyte (only 0.1 M KPF_6/MeCN). More experimental details can be found in the supporting information. Figure S1c (Supporting Information) displays the comparison between the CV responses measured with and without $K_5\{V_{12}\}$ in the potential window of −750 to 750 mV versus Ag^+/Ag. In the absence of $K_5\{V_{12}\}$, the measured CV response exhibits a charge storage behavior that is completely non-faradaic and without any redox features. This confirms that there are no redox-active species in the electrolyte. As a result, after nine consecutive cycles, no obvious changes were visible in the LIG electrode's CVs. In contrast, in the presence of $K_5\{V_{12}\}$ in the supporting electrolyte, the first cycles showed multiple redox peaks due to cluster reduction on the LIG surface. Notably, the

LIG electrode with dissolved $K_5\{V_{12}\}$ exhibited two broad peaks after nine CV cycles at a reduction potential (E_1) of −300 and an oxidation potential (E_2) of 600 mV versus Ag^+/Ag, confirming quasi-reversible charge storage. Consequently, the substantial increase in the area under the CV curve signifies a noteworthy alteration in the electrochemical performance of the LIG electrode due to $K_5\{V_{12}\}$ deposition at a higher overpotential within the range of −750 to 750 mV versus Ag^+/Ag.

Next, the possible changes in the electrode morphology upon $K_5\{V_{12}\}$ deposition were analyzed by scanning electron microscopy (SEM). The surface of the pristine LIG electrode is shown in Figure S2a,b (Supporting Information), emphasizing its highly porous morphology, which is essential for the diffusion and deposition of the $K_5\{V_{12}\}$ cluster into the LIG pores upon application of cathodic potential. Figure S2c,d (Supporting Information) shows the morphology of the as-synthesized K-POV-750 electrode, revealing that the porous nanostructure of the LIG surface remains intact post-cluster deposition, with no visible aggregation of the clusters or electrolyte salt. The ultrathin, flakes-like morphology and porous nanostructure of the LIG substrate confer superior mechanical properties. Despite the $K_5\{V_{12}\}$ deposition, the LIG surface retains its inherent mechanical properties, including the retention of electronically conductive channels and a microporous architecture that facilitates enhanced electron mobility and ionic conductivity. To gain a deeper understanding of the elemental composition and validate the deposition of $K_5\{V_{12}\}$ on the LIG carbon structure, energy dispersive X-ray (EDX) spectroscopy analysis was performed for all three synthesized electrodes (K-POV-250, K-POV-500, and K-POV-750, Figure S2e-g, Supporting Information). The results confirmed the presence of the primary cluster components, vanadium (V) and potassium (K), for all synthesized electrodes. The EDX elemental analysis also revealed a slight variation in the K:V ratio, likely due to the different applied potential ranges (Table S1, Supporting Information). Therefore, the range of applied potential has a notable influence on the $K_5\{V_{12}\}$ deposition, allowing for plausible variations in the ratio of vanadium to potassium for the three synthesized samples.[37] X-ray diffraction (XRD) measurements were performed to evaluate the influence of the deposited $K_5\{V_{12}\}$ cluster on the LIG surface, as shown in Figure S2h (Supporting Information). The LIG electrode defined a distinct peak at a 2-theta value of ≈26°, corresponding to the (002) plane, which indicates a high degree of graphitization in the fabricated LIG substrate.[41] For all $K_5\{V_{12}\}$ modified electrodes, the observed peak at 26° became less prominent and gradually deteriorated with the cluster deposition at a higher potential range, confirming that the LIG structure is significantly altered by the deposition of $K_5\{V_{12}\}$ nanocluster.

Raman spectroscopy was employed to gain insights into changes in structural and electronic properties of the LIG substrate resulting from $K_5\{V_{12}\}$ deposition. The micro-Raman spectrum of pristine LIG is presented in Figure S3 (Supporting Information). Three prominent Raman bands at ≈1350 cm^{-1}, 1586 cm^{-1}, and 2695 cm^{-1} are recognized as the D, G, and 2D bands, respectively, which are commonly associated with any graphitic lattice.[42] The D band is attributed to phonons related to defects in the sp^2-carbon lattice, the G band signifies symmetric stretching of the sp^2-carbon lattice, and the 2D band originates from second-order zone-boundary phonons. The D' band, positioned at ≈1620 cm^{-1}, is also a vibrational mode related to defects and is observed as a shoulder band to the G band. It is commonly accepted that the ratio of peak intensities I_D/I_G is a measure for the disorder in the graphite layers, and the observed value of 0.72 for LIG suggests a nanocrystalline nature of the graphitic lattice.[43] Furthermore, the full width at half maximum (FWHM) of the 2D band (≈62 cm^{-1}) and the I_{2D}/I_G ratio (0.49) indicate that the pristine LIG primarily consists of randomly oriented stacks of graphene layers.[44] In addition, the presence of Raman bands such as D'' (≈1100 cm^{-1}), D' (≈1620 cm-1), D+D″ (≈2450 cm^{-1}), and D+D' (≈2940 cm^{-1}) also corroborates the presence of defective graphene lattices.[45] Given that the electrical conductivity and ion mobility of graphitic material depends on the structural properties of the sp^2 lattice, it is necessary to quantify changes in the number of defects during the electrochemical deposition of $K_5\{V_{12}\}$ and assess the overall crystallinity of the LIG electrode after cycling.

Defects within a graphite lattice can be classified into two categories: point-like defects (such as sp^3-type, vacancy-like defects, Stone-Wales defects, etc.) and line-like defects (including dislocations, grain boundaries, etc.). The quantification of defects in the graphitic lattice involves examining I_D/I_D' and D bandwidth with respect to the G-band-width.[45,46] In order to gain a better understanding of the distribution of defects in the graphitic lattice of the pristine LIG surface, Raman imaging measurements were carried out (with a spatial resolution of 1 × 1 mm^2 in a 60 × 60 mm^2 region). The results were put together in maps showing the peak intensities, positions, and widths (FWHM) of the D, G, and D' bands (Figure S4a, Supporting Information) and in histograms (Figure S4b, Supporting Information). The G band ranged from 1568 to 1586 cm^{-1}, and the D band from 1335 to 1348 cm^{-1}. It has been shown in literature that a red-shift of the bands together with a higher FWHM indicates the defect-rich regions of the LIG surface.[43,46] A prior investigation on defect-rich graphene concluded that the I_D/I_D' ratio is ≈13 for sp^3-type defects, ≈7 for vacancy-type defects, and 3.5 for boundary-type defects.[45] In our case, the pristine LIG exhibited an I_D/I_D' ratio of 3.69, suggesting a substantial influence of grain boundary-type defects on the nano-graphitic structure of LIG.[43,45] **Figure 2a** presents the development of characteristic values of the Raman spectra, namely peak positions (D, G, and D' band), FWHM of these bands, and $I_D/I_{D'}$ peak intensity ratio for pristine LIG, K-POV-500, and K-POV-750 electrodes. These values were derived by averaging the results of Raman maps. While the average peak frequency of all bands remains relatively constant, the FWHM and I_D/I_D' values exhibit a declining trend for $K_5\{V_{12}\}$ deposition at increasing overpotential. Furthermore, the decrease of the I_D/I_D' ratio after $K_5\{V_{12}\}$ deposition from 3.69 (pristine LIG) to 2.88 and 2.66 for K-POV-500 and K-POV-750 electrodes, respectively, signifies the elimination of grain boundary defects in the nano-graphite lattice, presumably leading to an improvement of the electrochemical properties of LIG. Additionally, the absence of sp^3-like defects or vacancies in LIG points to a predominant physisorption of the electrochemically deposited $K_5\{V_{12}\}$ on the LIG surface. Consequently, the deposited and reduced $K_5\{V_{12}\}$ does not form direct covalent or ionic bonds with the graphitic lattice.

Coming to the discussion of vanadate species, corresponding Raman spectra of pure $K_5\{V_{12}\}$ and K-POV-500 and K-POV-750

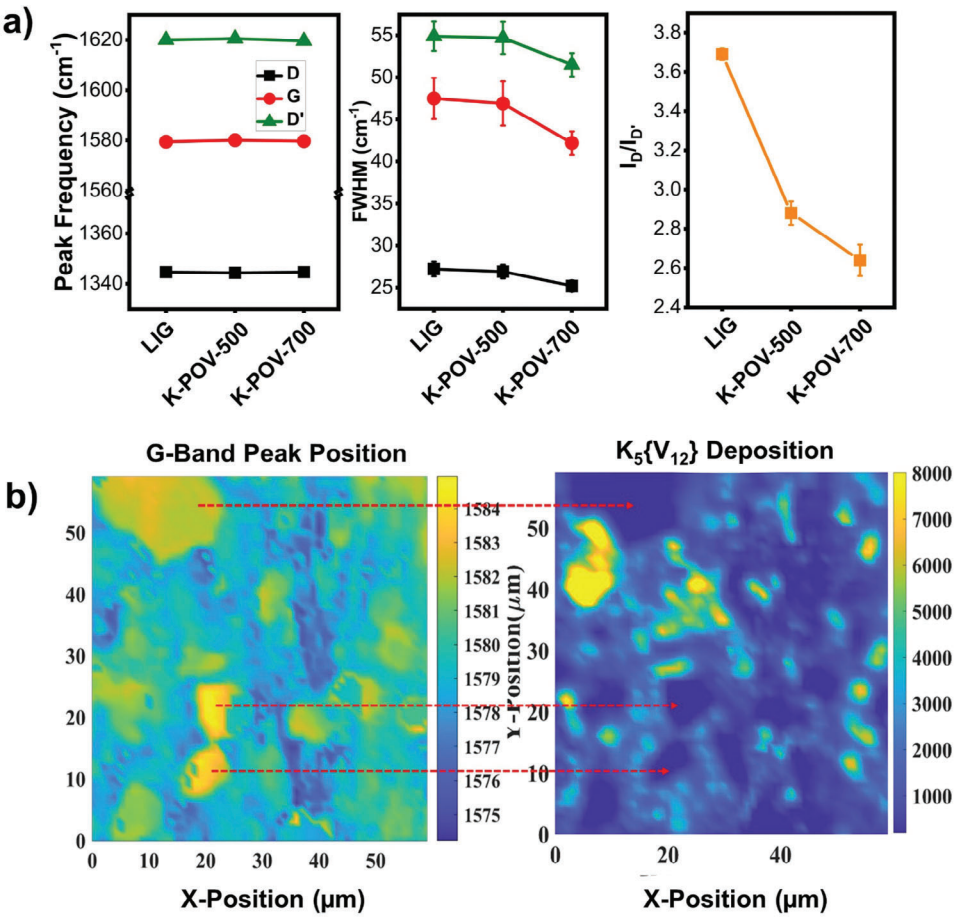

Figure 2. a) Comparison of Raman band parameters of unmodified LIG with K-POV-500 and K-POV-750 electrodes. b) Raman mapping of G band peak position and $K_5\{V_{12}\}$ deposition (from the intensity of the V-O stretch vibration at 875 cm^{-1}) for the synthesized K-POV-750 electrode, illustrating preferential deposition in the regions of low crystallinity.

electrodes are depicted in Figure S5a (Supporting Information). The intense band at ≈875 cm^{-1}, along with weaker bands at ≈938 cm^{-1} and 995 cm^{-1}, corresponds to the stretching vibration of VO_6/VO_5 units forming the polyoxovanadates.[47] Lower frequency bands at 400–600 cm^{-1} are generally assigned to the stretching vibrations of terminal V-O linkages, while bands at 200–400 cm^{-1} are associated with V-O-V bending modes. First of all, the detection of the band at ≈875 cm^{-1} confirms the presence of $K_5\{V_{12}\}$ on the K-POV-500 and K-POV-750 electrodes. Furthermore, the mapping result of this peak for the K-POV-500 electrode (Figure S5c, Supporting Information) reveals a heterogeneous spatial distribution of $K_5\{V_{12}\}$ on the surface. In addition, comparing this mapping result with that of the G-band peak position shows that $K_5\{V_{12}\}$ is preferentially situated around the regions with higher G-band peak frequencies, which are related to a higher crystallinity in the graphitic lattice (see above). Hence, the results demonstrate that electrochemical deposition favors the less crystalline regions of the LIG surface, although deposition starts initially rather at the boundary between the low- and high-crystalline regions. The mapping result for K-POV-750 exhibits a similar trend (Figure 2b), with preferred $K_5\{V_{12}\}$ deposition in the low crystallinity regions. This noteworthy behavior of preferential deposition provides further insight into the physiochemical nature of the fabricated LIG. In this context, the pristine crystalline segments of LIG maintain high electrical and ionic mobility, while the sections with deposited $K_5\{V_{12}\}$ in K-POV-750 and K-POV-500 modified the chemical inertness of the sp^2 lattice in LIG.

In the next step, X-ray photoelectron spectroscopy (XPS) was used to test the elemental composition and the chemical state of the elements in the surface layer. The results of measurements of pristine samples (LIG and K-POV-750) before cycling are shown in Figure S6 (Supporting Information). The survey spectrum of pure LIG shows dominating signals of carbon (C1s peak at ≈285 eV) and oxygen (O1s peak at ≈532 eV) (Figure S6a, Supporting Information). As expected, the deposition of $K_5\{V_{12}\}$ leads to additional features in the survey spectrum of K-POV-750, which can be attributed to potassium (K2p peak at ≈293 eV) and vanadium ($V2p_{3/2}$ peak at ≈517 eV). The detailed spectrum in the C1s region shows for pure LIG the typical features of a graphitic sample, with the dominating sp^2-C peak at 284.5 eV and the π-π^* satellite at 290.9 eV (Figure S6b, Supporting Information).[49] In addition, relatively prominent peaks at 285.1 eV, 286.6 eV, and 288.3 eV point to sizable quantities of C-C/C-H, C-O, and

C = O species on the surface, respectively. In agreement with the results in the C1s region, the main peaks in the O1s spectrum (Figure S6c, Supporting Information) are assigned to C = O (531.9 eV) and C-O (533.1 eV) groups, respectively. The C1s detail spectrum of K-POV-750 (Figure S6d, Supporting Information) shows the same C species as the pure LIG. The stronger reduction of the intensities of the C-C/C-H, C-O, and C = O contributions compared to the sp^2-C signal corroborates the preferential deposition of $K_5\{V_{12}\}$ clusters on defect sites. The C1s spectrum also includes the K2p peak doublet of the K-POV with the $K2p_{3/2}$ peak component at 293.3 eV. Similarly, the O1s and V2p peaks of K-POV-750 appear in one common binding energy region (Figure S6e, Supporting Information). The peak fit shows that most vanadium is in oxidation state +V ($V2p_{3/2}$ peak at 517.6 eV); in addition, a smaller contribution from V^{+IV} ($V2p_{3/2}$ peak at 516.3 eV) can also be discerned. For oxygen, the additional peak at 530.3 eV can be assigned to the POV oxygen atoms. The results of the quantitative analysis of pure LIG and the three K-POV electrodes are compiled in Table S2 (Supporting Information). A comparison of the K-POV electrodes shows for K-POV-750 the highest V concentration; hence, $K_5\{V_{12}\}$ deposition seems to be most effective for the largest potential window.

To investigate the electrochemical performance of pristine LIG and $K_5\{V_{12}\}$ deposited electrodes, we first performed cyclic voltammetry measurements in a typical three-electrode cell setup at a set operating potential referenced to the standard Ag/AgCl electrode (aqueous reference), using a Pt wire as counter electrode and aqueous 1 M H_2SO_4 as electrolyte. The operating potential window for the measurement ranged from −300 to 1000 mV (versus aq. Ag^+/Ag). The detailed experimental procedures are described in the supporting information. The CV curves shown in **Figure 3a** indicate that all K-POV electrodes exhibit significantly improved cyclic voltammetry responses compared to pristine LIG electrode, and thus enhanced charge storage capacity. As confirmed by Raman mapping (see above), the $K_5\{V_{12}\}$ cluster deposition preferentially takes place at regions of low crystallinity on the LIG electrode, which seems to contribute to the improved electronic and electrochemical properties of the graphitic structure. Controlled CV measurements were performed on the pristine LIG electrode in 1 M H_2SO_4 electrolyte containing the $K_5\{V_{12}\}$ cluster and showed a broad reduction peak in the range of 600–800 mV versus Ag^+/Ag, without an enhancement of the overall capacitance of LIG as in the case of K-POV modified electrodes (see Figure S7, Supporting Information). This confirms that the deposition of $K_5\{V_{12}\}$ on the LIG surface is a crucial step for the enhanced electronic and electrochemical properties of the LIG electrodes. Among all electrodes, the K-POV-750 electrode with greater content of deposited $K_5\{V_{12}\}$ demonstrates the best overall charge storage supercapacitive performance with the highest specific areal capacitance C_A (38.49 mF cm^{-2}) at a scan rate of 10 mV s^{-1}. In contrast, the undoped LIG electrode shows substantially lower C_A (approximately 10.68 mF cm^{-2}). Therefore, all other electrochemical measurements were carried out on K-POV-750 electrodes. Figure 3b illustrates the stable performance of the K-POV-750 electrode at different scan rates ranging from 10 to 100 mV s^{-1}, indicating its suitability for various operating conditions.

Next, to validate the enhanced electrochemical efficacy of the K-POV-750 electrode, the galvanostatic charge-discharge (GCD) response was recorded at various current densities ranging from 0.1 to 2 mA cm^{-2} as illustrated in Figure 3c. The GCD curves display a quasi-linear charge-discharge profile, affirming the excellent reversible supercapacitive behavior at different current densities. The K-POV-750 electrode exhibited the highest areal capacitance of 125 mF cm^{-2} at a current density of 0.1 mA cm^{-2}, a significant improvement compared to the pristine LIG electrode, which achieved a maximum areal capacitance of 25 mF cm^{-2}, i.e., only one-fifth of the K-POV-750 electrode, as depicted in Figure 3d. Similarly, the other two synthesized electrodes K-POV-500 and K-POV-250 delivered areal capacitances of 48 and 26 mF cm^{-2}, respectively, at 0.1 mA cm^{-2} (Figure 3d; Figure S8, Supporting Information). This outcome implies superior capacitive performance when the $K_5\{V_{12}\}$ molecular nanocluster was deposited on the LIG surface within a comparatively wide potential range, significantly influencing the overall electrochemical performance of the synthesized electrode. Presumably, the electrochemical deposition of the $K_5\{V_{12}\}$ within this enhanced potential window delineated the structural and chemical modification of the LIG, favoring the fast reversible Faradic response between the electrolyte and $K_5\{V_{12}\}$ modified LIG nanostructure.[50] This structural modification on the LIG surface promotes a vanadium oxide framework complex, facilitating reversible interaction/de-insertion of electrolyte ions during charging and discharging.[47,48] Additionally, the poor electrochemical performance at higher current density is in agreement with the high internal resistance, i.e., equivalent series resistance (ESR), which can be directly measured from the voltage drop V_{ESR} during the GCD cycles.[51] At a current density of 1 mA cm^{-2}, the calculated V_{ESR} for the K-POV-750 electrode is 260 mV, whereas the pristine LIG electrode exhibits a significantly higher V_{ESR} value of 1204 mV (Figure 3e). Similarly, the synthesized K-POV-500 and K-POV-250 electrodes show V_{ESR} values of 386 and 436 mV, respectively, indicating low internal resistance for the synthesized electrodes (Figure S8, Supporting Information).

To gain insight into the detailed charge storage process, the charge storage kinetics of the synthesized electrodes were explored during cyclic voltammetry sweeps. The calculated specific capacitance was interpreted quantitatively, revealing two distinct processes: the electric double-layer capacitance (EDLC), primarily a non-faradaic current response derived from capacitive performance, and the diffusion-controlled current arising from faradaic intercalation and deintercalation of the electrolyte ions, estimated by Dunn analysis.[52] The current response (I) at a fixed potential (V) is attributed to these two different charge storage mechanisms and can be expressed as:

$$I(V) = k_1 v + k_2 v^{1/2} \quad (1)$$

where v is the scan rate, $k_1 v$ defines the non-faradaic process and $k_2 v^{1/2}$ represents the diffusion-controlled contribution.[53,54] Figure 3f illustrates the voltage profile of the synthesized K-POV-750 electrode (at 10 mV s^{-1}), depicting the magnitude of the two charge storage contributions. At 10 mV s^{-1}, 95.5% of the observed current is contributed by the diffusion-controlled mechanism, showcasing significantly improved localized ion diffusivity to the carbon channel, while only a minor current response is associated with the EDLCs' capacitive behavior. Comparative analysis with the other two synthesized electrodes

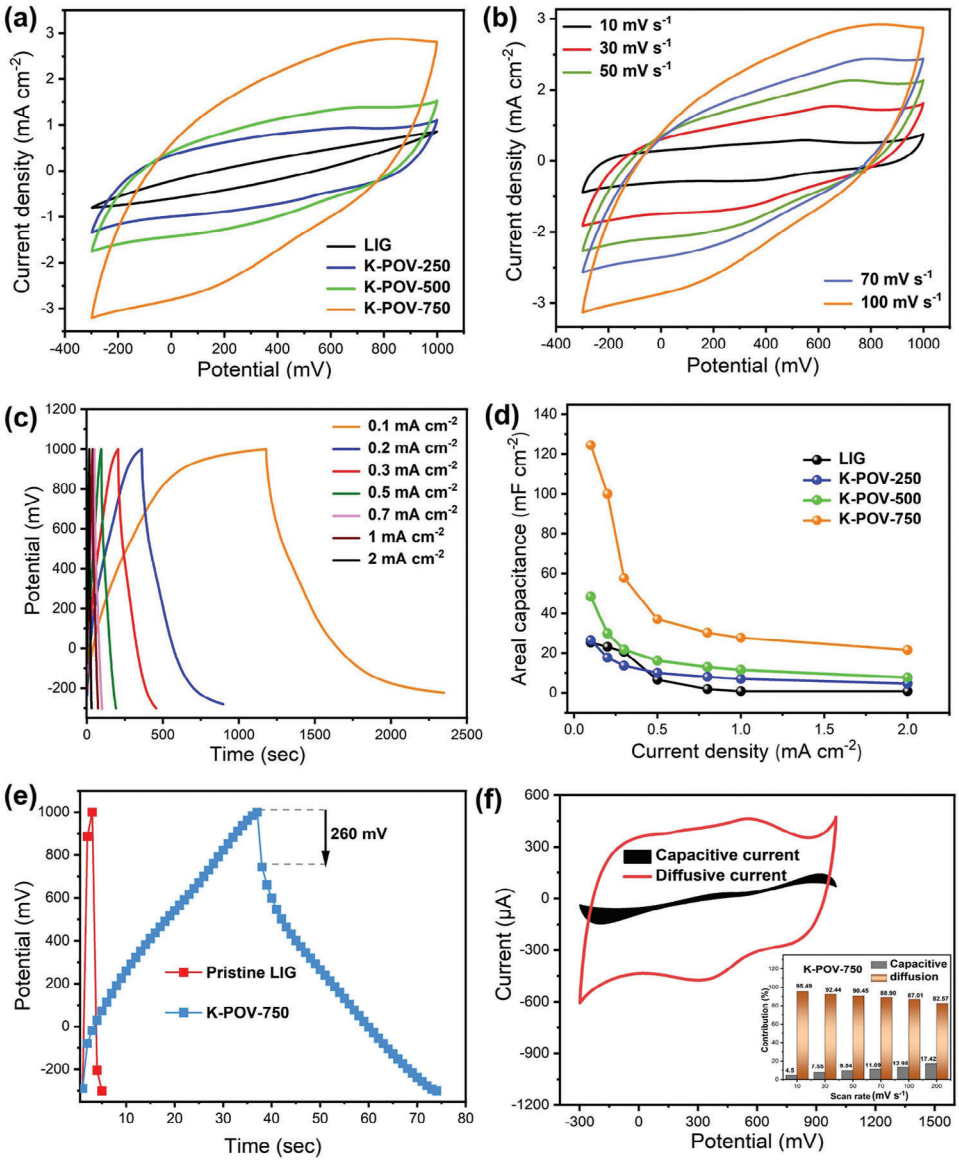

Figure 3. a) Cyclic voltammograms of K-POV-250, K-POV-500, and K-POV-750 electrodes compared with pristine LIG electrode b) CV response of K-POV-750 electrode at different scan rates from 10 mV s^{-1} to 100 mV s^{-1} c) galvanostatic charge-discharge profiles of K-POV-750 electrode at various current densities from 0.1 to 2 mA cm^{-2} d) areal capacitance (C_A) of the synthesized electrodes at different current densities e) voltage drop V_{ESR} profile of K-POV-750 and LIG electrode at 1 mA cm^{-2} and f) quantitative analysis of charge storage mechanism of K-POV-750 electrode at 10 mV s^{-1} (inset: diffusion and capacitive controlled current response at different scan rates).

(K-POV-250 and K-POV-500) suggests a predominant charge storage contribution due to the capacitive performance of the electrode when cycled from lower to higher scan rates (Figure S9, Supporting Information).

The concept's validity was ultimately shown by assembling a flexible solid-state supercapacitor (SSC-KPOV-750) using two symmetrical K-POV-750 electrodes with PVA-H_2SO_4 gel electrolyte and laboratory-grade micropores tissue paper as a separator, as illustrated in **Figure** 4a. In this study, the performance of SSC-KPOV-750 was compared with a similar SSC-LIG device based on pristine LIG electrodes. The CV performance of SSC-KPOV-750 at different scan rates, ranging from 10 to 100 mV s^{-1}, is presented in Figure 4b. The fabricated device has better pseudocapacitive performance compared to SSC-LIG, as indicated by a quasi-reversible CV within the potential range from −300 to 1000 mV. The stability of the synthesized SSC-KPOV-750 device was evaluated with the obtained CV curves at different scan rates from 10 to 100 mV s^{-1}. The two pronounced broad peaks at ≈200 and 550 mV versus Ag^+/Ag (at 30 mV s^{-1}) represent the reversible faradic reaction, contributing to excellent charge storage behavior even at a higher scan rate. Additionally, the CV of pristine SSC-LIG at 100 mV s^{-1}, when compared with SSC-KPOV-750, demonstrates significantly inferior charge storage behavior (Figure 4c). The GCDs curve for SSC-KPOV-750 (Figure 4d, Supporting Information) exhibits non-linear, asymmetrical profiles, indicative of capacitive behaviour attributed to

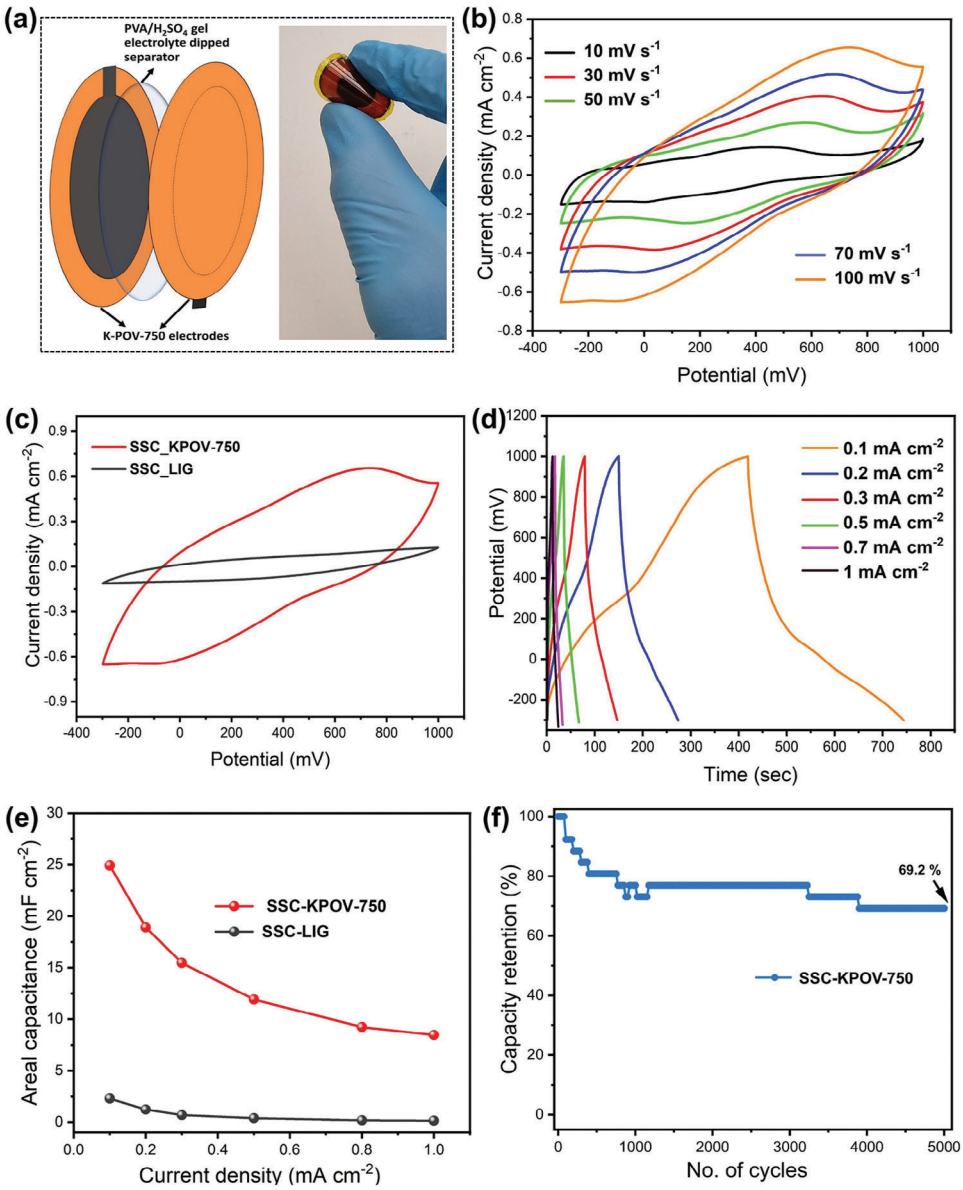

Figure 4. a) Schematic illustration of fabricated SSC-KPOV-750, inset: image of real flexible supercapacitor device; b) CV curves for SSC-KPOV-750 at different scan rates from 10 to 100 mV s^{-1}; c) comparison of the CV curve at 100 mV s^{-1} for SSC-KPOV-750 and SSC-LIG; d) GCD profiles of SSC-KPOV-750 at different current densities from 0.1 to 1 mA cm^{-2}; e) specific areal capacitance of SSC-KPOV-750 and SSC-LIG at various current densities; and f) cycling performance of SSC-KPOV-750 device during 5000 cycles at 0.8 mA cm^{-2}.

reversible Faradaic response occurring at the electrode-electrolyte interphase. For comparison, the GCD profiles of pristine LIG-based SSCs reveal a relatively short charge-discharge duration for current densities in the range from 0.1 to 0.5 $mAcm^{-2}$ (Figure S10, Supporting Information). The total areal capacitance for SSC-KPOV-750 is 24.92 mF cm^{-2} at a current density of 0.1 mA cm^{-2}, ≈11 times higher than that of the pristine LIG-based SSC (Figure 4e). Similarly, at the higher current density of 1 mA cm^{-2}, the SSC-KPOV-750 sustains a decent performance of C_A ≈8.5 mF cm^{-2}, whereas the SSC-LIG exhibits instability after 0.5 mA cm^{-2} (C_A<< 1 mF cm^{-2}) due to a high internal resistance. These results confirm the better rate capability of the SSC-KPOV-750. Furthermore, the cycling stability of the SSC-KPOV-750 device was evaluated through 5000 consecutive charge-discharge cycles performed at 0.8 mA cm^{-2}, as depicted in Figure 4f.

The SSC-KPOV-750 device exhibits an initial capacity fade of ≈20% over the first few hundred cycles, potentially due to the initial activation of the electrode surface. Over the subsequent 4000 cycles, capacity fade was limited to 7%, maintaining a stable capacitive performance with 69% capacity retention. However, minor fluctuation observed at the 3200th and 4000th cycles correspond to random ruptures or crack formations within the carbon microstructure. Figure S10c (Supporting Information) presents the Ragone plot that compares the areal power density (mW cm^{-2}) and energy density (mWh cm^{-2}) of both SSC-LIG

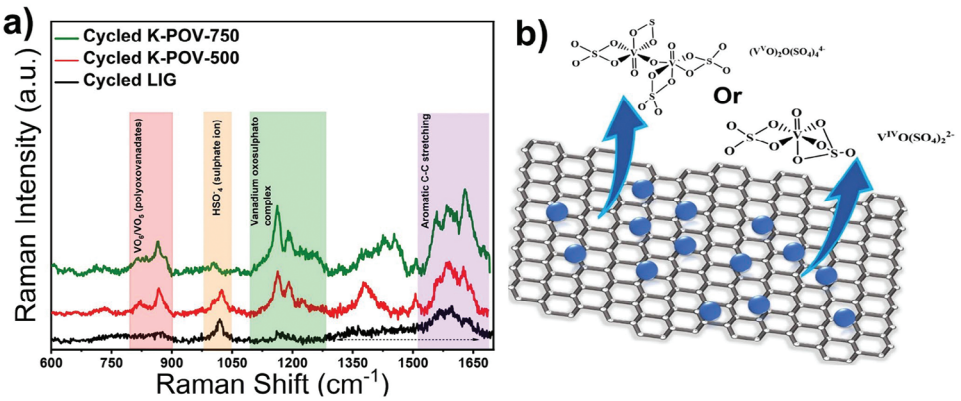

Figure 5. a) Raman spectra of LIG, K-POV-500, and K-POV-750 electrodes after 50 CVs. b) Schematic representation of the dimeric and monomeric vanadium oxosulphato complexes formed during electrochemical cycling.

and SSC-KPOV-750. The SSC-KPOV-750 had the highest areal energy density of 5.68 mWh cm^{-2} at a power density of 0.063 mW cm^{-2}, which was over 10 times more than that of SSC-LIG. Electrochemical impedance spectroscopy (EIS) measurements were conducted to comprehend the overall impedance of the fabricated solid-state devices. The Nyquist plot obtained over a frequency range from 1 Hz to 1 MHz for both SSC-KPOV-750 and SSC-LIG is shown in Figure S10d (Supporting Information). The plot of SSC-KPOV-750 consists of an almost straight line in the low-frequency region, indicative of ideal electric double-layer (EDL) capacitive behavior, while SSC-LIG displays a large Warburg response, suggesting high charge transfer resistance. Finally, the experimental data was fitted with an equivalent circuit to assess the charge transfer mechanism, with R_1 and R_2 representing the solution resistance (R_S) and charge transfer (R_{CT}), respectively. Notably, these resistances are significantly lower for SSC-KPOV-750 compared to SSC-LIG, as shown in Figure S10e,f (Supporting Information). Next, the mechanical flexibility test was conducted for the fabricated SSC-KPOV-750 device at different bending positions as shown in Figure S11 (Supporting Information). The capacitance exhibited minor variations at the initial bending angle and maintained nearly 94.2% of its original capacitance value, thereby demonstrating superior electrochemical performance and mechanical stability. These results indicate that the electrodeposited polyoxovanadates ($K_5\{V_{12}\}$) complexes were effectively introduced into the porous graphene structure and contributed to the long-term stable electrochemical performance of the SSC-KPOV-750 device.

The observed electrochemical responses of synthesized K-POV-750, K-POV-500, and K-POV-250 electrodes suggest that the deposition of reduced cluster $K_5\{V_{12}\}$ within a specific potential range enhances the electrochemical activity of the LIG electrodes. Therefore, it is important to understand the morphological and structural changes occurring in these modified electrodes during electrochemical cycling in an acidic aqueous electrolyte (1 M H_2SO_4) and compare them with the pristine LIG. We performed a post-mortem analysis of cycled K-POV-750, K-POV-500, and LIG electrodes (details of the preparation of the electrodes after cycling are given in the SI). We assessed the changes in the chemical composition of cycled electrodes by Raman and XPS analysis after performing an initial 50 CV sweeps. First, the Raman spectra of the pristine LIG electrode after cycling reveal a complete loss of the characteristic D and G bands observed in the fresh LIG electrode (**Figure 5a**). Instead, a broad Raman feature ranging from 1300 cm^{-1} to 1660 cm^{-1} is evident, resembling a highly amorphous soot-like carbon structure.[55] The electrochemical cycling in aqueous electrolyte (1 M H_2SO_4) induces oxidation of the graphitic lattice, resulting in the formation of sp^3-type defects and causing a transformation of LIG into an amorphous phase. Moreover, the distinct Raman band at ≈1019 cm^{-1} can be attributed to the stretching vibration of HSO_4^-, either intercalated or covalently bonded to the layers of LIG.[56] This substantial chemical transformation during electrochemical cycling can be interpreted as the manifestation of supercapacitive behavior in LIG.

The Raman spectra acquired from the cycled electrodes K-POV-750 and K-POV-500 (Figure 5a) reveal distinctive chemical transformations during cycling. First of all, the pronounced and convoluted Raman bands ≈1500–1650 cm^{-1} can be attributed to aromatic C-C stretching. Compared to pure LIG, two new bands at 817 cm^{-1} and 867 cm^{-1} are detected, corresponding to the polyoxovanadate VO_6/VO_5 units. It is noteworthy that these bands exhibit a red shift compared to the corresponding intense band (875 cm^{-1}) of the K-POV electrodes before cycling (Figure S5a, Supporting Information), likely due to the reduction of the vanadium core in VO_6/VO_5.[47] Additionally, a combination of bands occurs for both K-POV electrodes in the range of ≈1110-1270 cm^{-1}, with two prominent peaks at ≈1162 cm^{-1} and 1190 cm^{-1}, absent in the cycled LIG electrode (Figure S12, Supporting Information). These bands can be assigned to various vanadium oxosulphato/hydroxysulphato complexes which are formed during electrochemical cycling in 1 M H_2SO_4. Previous studies on vanadium redox flow batteries have demonstrated that the thermal stability and kinetics of the electrolyte ($VOSO_4$/3.0 M H_2SO_4) can be enhanced by organic additives with sulphonic acid (-SO_3H) or amine (-NH_2) groups.[57] It is established that the sulphate and sulphonic acid groups form solvated complexes with vanadium oxide under acidic conditions.[57] Furthermore, sulphates are able to form different types of vanadium oxosulphato complexes when vanadium oxide (V_2O_5) is melted with sulphate-containing salts.[58] In the presence of potassium sulphate, vanadium oxide forms dimeric $(V^VO)_2O(SO_4)_4^{4-}$ with a V-O-V bridge and a reduced monomeric $V^{IV}O(SO_4)_2^{2-}$ as shown

in the schematic in Figure 5b.[58,59] It seems plausible that the deposited and reduced $K_5\{V_{12}\}$ clusters might undergo a similar complex formation at high electrochemical potential in 1 M H_2SO_4 medium. Consequently, the Raman bands at 1190 cm^{-1} and 1162 cm^{-1} can be associated with the V^V-oxosulphato and the V^{IV}-oxosulphato complexes, respectively.[58] Interestingly, the hydrogen sulfate ion (HSO_4^-) peak at 1020 cm^{-1} is quite prominent in the Raman spectrum of the cycled K-POV-500 electrode, while it is rather weak for K-POV-750. Taken together, the electrochemical potential window along with prolonged cycling leads to a transformation of the polyoxovanadate structure to a mixture of vanadium oxosulphato complexes with V^V or V^{IV} centers.

XPS measurements were also carried out on samples that were recovered after the initial 50 CV cycles, the results for the cycled LIG and K-POV-750 electrodes are displayed in Figure S13 (Supporting Information). Starting with the LIG electrode, the detail spectrum in the C1s region shows a strong decline of the sp^2-C peak (at 284.5 eV) and the π-π^* satellite. In contrast, a strong increase in the hydrocarbon peak (C-C/C-H at 285.1 eV) is observed. These results point to a loss of graphitic material in the surface layer of the LIG electrode during electrochemical cycling, either due to reaction/etching of the graphite material by the sulphuric acid-containing electrolyte or deposition of carbonaceous species from the electrolyte. A similar development is also observed in the C1s spectrum of the K-POV-750 electrode, although the reduction of the intensity of the sp^2-C peak (and the π-π^* satellite) is not so pronounced in this case. Interestingly, the measurements for this sample showed that the vanadium and potassium content in the surface layer accessible by XPS (≈5 – 10 nm) is below the detection limit of XPS (≈0.1 to 0.3 at-% for these two elements). Since the Raman measurements demonstrated that vanadium oxides are still present in the electrodes after cycling, this finding is further evidence for the formation of a surface interlayer during cycling which covers the graphite substrate and the vanadium oxide clusters. While the S2p spectrum of cycled LIG shows a single S2p peak doublet ($S2p_{3/2}$ at 169.5 eV) which can be assigned to hydrogen sulphates/sulphates, two doublets can be discerned for K-POV-750 ($S2p_{3/2}$ at 163.9 and 168.6 eV, respectively) indicating the additional presence of reduced species in the surface layer of this sample. The oxygen atoms in the hydrogen sulphates/sulphates also contribute to the detail spectra in the O1s region. From a comparison of the peak intensities, it seems that this additional intensity goes mainly into the C-O peak at 533.0 eV. Since the O1s peak of metal sulphates is usually found at ≈531.5 eV, while the signals of hydrogen sulphates appear ≈533 eV, it follows that mainly hydrogen sulphates are captured in the surface layer of the electrodes.

A detailed post-mortem analysis of the aged SSC-KPOV-750 electrode was conducted after 5000 electrochemical cycles. At first, the morphology of the aged electrode surface was examined using the SEM analysis, which revealed a microstructure nearly identical to that of a fresh electrode, resulting in outstanding electrochemical reversibility as shown in Figure S14a,b (Supporting Information). The micro-Raman spectra gain more insight into the structural changes that occurred in the electrode after prolonged cycling, as depicted in Figure S14c (Supporting Information). The characteristic Raman band of native $K_5\{V_{12}\}$ at ≈875 cm^{-1} remained detectable, indicating the persistence of polyoxovanadate even after extensive cycling. Additionally, the spectra revealed the presence of other vanadium oxosulphato complexes with V^V or V^{IV} centers, marked by bands at 1162 and 1190 cm^{-1}, further confirming the presence of vanadium complexes. A notable Raman band at ≈1019 cm^{-1} indicated a strong interaction between sulphate ions of the electrolyte and the LIG structure. Furthermore, the XPS result of the aged K-POV-750 electrode indicated the well-maintained intensity of the sp^2-C peak and the π-π^* satellite is still observable, as confirmed by the high-resolution C1s spectrum (Figure S14e, Supporting Information). The S2p spectrum showed a single S2p peak doublet ($S2p_{3/2}$ at 169.5 eV), representing the predominated presence of hydrogen sulphates/sulphates on the electrode surface (Figure S14g, Supporting Information). However, the chemical composition of vanadium and potassium on the surface layer of the aged electrode remained undetermined due to the detection limit of XPS as described earlier, a limitation also noted for the partially cycled K-POV-750 electrode.

3. Conclusion

In summary, our study demonstrates the effective electrochemical immobilization of the potassium-bridged vanadium oxide nanocluster $K_5\{V_{12}\}$ on a highly porous graphene-like LIG substrate through a straightforward cyclic voltammetry technique. The electrochemical deposition of the nanoclusters within different potential ranges corresponds to distinct electronic and electrochemical changes in the LIG electrodes. The optimum POV deposition was achieved for electrodeposition in a potential range of −750 to 750 mV versus Ag^+/Ag, which leads to the presence of a highly redox-active and stable reduced cluster species on the LIG surface. This process also fine-tunes the electrochemical active sites on the graphene surface. The resulting K-POV-750 electrode exhibits a superior areal capacity of 125 mF cm^{-2} at a current density of 0.1 mA cm^{-2}. In comparison, the unmodified LIG electrode delivers an areal capacity of 25 mF cm^{-2} at 0.1 mA cm^{-2}. Detailed Raman measurements and XPS analysis provide insights into the deposition of POV clusters at different potential ranges and possible structural and material modifications of the LIG surface. Raman mapping reveals preferential deposition of $K_5\{V_{12}\}$ clusters in low crystallinity regions which enables high electronic conductivity of LIG after deposition. At the same time, detailed Raman analysis on the modified K-POV-750 electrode reveals the oxidation of surface sp^2 carbon centers. The deposited $K_5\{V_{12}\}$ clusters also transformed to dimeric V^V or monomeric V^{IV} polyoxovanadate centers on the modified electrode surface. Furthermore, the performance of the modified K-POV-750 electrode was evaluated in a symmetrical real supercapacitor device assembled with PVA/H_2SO_4-based gel electrolyte. The flexible symmetrical supercapacitor (SSC) with K-POV-750 sustains excellent electrochemical response with an areal capacitance of 24.92 mFcm^{-2} (at 0.1 mA cm^{-2}) and good capacity retention of 69% for up to 5000 charge-discharge cycles. The SSC-KPOV-750 device delivers an energy density of 5.68 mWh cm^{-2} and a power density of 0.063 mW cm^{-2}. In summary, this work presents a sustainable approach for introducing a highly redox-active potassium-bridged polyoxovanadate nanocluster into a graphene-like LIG framework, enhancing structural stability and improving electrochemical performance. The findings hold promise for applications in

micro-flexible smart devices, particularly in the fabrication of flexible micro-supercapacitors, without binders or current collectors.

4. Experimental Section

The experimental procedures and instruments used in this work are described in the supporting information

Supporting Information

Supporting Information is available from the Wiley Online Library or from the author.

Acknowledgements

This work contributes to the research performed at CELEST (Center for Electrochemical Energy Storage Ulm-Karlsruhe). Financial support by Ulm University, the Helmholtz-Gemeinschaft (HGF), and the Deutsche Forschungsgemeinschaft (DFG) within Germany's Excellence Strategy (EXC-2154/1), "POLiS" (project 390874152) and the TRR234 "CataLight" (project 364549901). M. A. thanks the State of Baden-Württemberg for a Margarete-von-Wrangell fellowship. The Baden-Württemberg Stiftung ("Elite program für Postdocs") is gratefully acknowledged. Dr. Monsur Islam is acknowledged for LIG electrode fabrication. The authors also acknowledge Dr. Bidhan Pandit for his contribution to Dunn's analysis.

Open access funding enabled and organized by Projekt DEAL.

Conflict of Interest

The authors declare no conflict of interest.

Data Availability Statement

The data that support the findings of this study are available from the corresponding author upon reasonable request.

Keywords

electrochemical deposition, flexible supercapacitors, laser-induced graphene, polyoxovanadates

Received: June 22, 2024
Revised: July 30, 2024
Published online:

[1] M. Horn, J. MacLeod, M. Liu, J. Webb, N. Motta, *Econ. Anal. Policy.* **2019**, *61*, 93.
[2] D. Wang, Y. Zhang, X. Lu, Z. Ma, C. h. Xie, Z. Zheng, *Chem. Soc. Rev.* **2018**, *47*, 4611.
[3] Z. Liu, H. Li, M. Zhu, Y. Huang, Z. Tang, Z. Pei, Z. Wang, Y. Huang, Z. Wang, Z. Shi, J. Liu, Y. Huang, C. Zhi, *Nano Energy* **2018**, *44*, 164.
[4] A. Colin, E. Ruppel, B. Lucia, In Proceedings of the Twenty-Third International Conference on Architectural Support for Programming Languages and Operating Systems, **2018**, 767.
[5] Y. Huang, W. S. Ip, Y. Y. Lau, J. Sun, J. Zeng, N. S. S. Yeung, W. S. Ng, H. Li, Z. Pei, Q. Xue, Y. Wang, J. Yu, H. Hu, C. Zhi, *ACS Nano* **2017**, *11*, 8953.
[6] Q. Ke, J. Wang, *J. Materiomics* **2016**, *2*, 37.
[7] S. Abdolhosseinzadeh, H. Asgharzadeh, H. S. Kim, *Sci. Rep.* **2015**, *5*, 10160.
[8] H. Zong, A. Zhang, J. Dong, Y. He, H. Fu, H. Guo, F. Liu, J. Xu, J. Liu, *Chem. Eng. J.* **2023**, *475*, 146088.
[9] Z. Lu, K. Zhao, H. Guo, L. Duan, H. Sun, K. Chen, J. Liu, *Small* **2024**, *20*, 2309814.
[10] A. Bahaa, M. A. Abdelkareem, A. Y. Mohamed, P. A. Shinde, B. A. A. Yousef, E. T. Sayed, H. Alawadhi, K.-J. Chae, S. Al-Asheh, A. G. Olabi, *J. of Colloid Interface Sci.* **2022**, *608*, 711.
[11] F. Clerici, M. Fontana, S. Bianco, M. Serrapede, F. Perrucci, S. Ferrero, E. Tresso, A. Lamberti, *ACS appl. Mater. Interfaces.* **2016**, *8*, 10459.
[12] J. Lin, Z. Peng, Y. Liu, F. Ruiz-Zepeda, R. Ye, E. L. G. Samuel, M. J. Yacaman, B. I. Yakobson, J. M. Tour, *Nat. Commun.* **2014**, *5*, 5714.
[13] C. Zhang, Z. Peng, C. Huang, B. Zhang, C. Xing, H. Chen, H. Cheng, J. Wang, S. Tang, *Nano Energy* **2021**, *81*, 105609.
[14] F. Clerici, M. Fontana, S. Bianco, M. Serrapede, F. Perrucci, S. Ferrero, E. Tresso, A. Lamberti, *ACS Appl. Mater. Interfaces* **2016**, *8*, 10459.
[15] Y. Zhang, L. Guo, S. Wei, Y. He, H. Xia, Q. Chen, H.-B. Sun, F.-S. Xiao, *Nano Today* **2010**, *5*, 15.
[16] R. Ye, D. K. James, J. M. Tour, *Adv. Mat.* **2019**, *31*, 1803621.
[17] C. Zhang, J. Chen, J. Gao, G. Tan, S. Bai, K. Weng, H. M. Chen, X. Ding, H. Cheng, Y. Yang, J. Wang, *Nano let* **2023**, *23*, 3435.
[18] F. M. Vivaldi, A. Dallinger, A. Bonini, N. Poma, L. Sembranti, D. Biagini, P. Salvo, F. Greco, F. D. Francesco, *ACS Appl. Mater. Interfaces* **2021**, *13*, 30245.
[19] C. Zhang, H. Chen, X. Ding, F. Lorestani, C. Huang, B. Zhang, B. Zheng, J. Wang, H. Cheng, Y. Xu, *Appl. Phys. Rev.* **2022**, *9*, 011413.
[20] M. Reina, A. Scalia, G. Auxilia, M. Fontana, F. Bella, S. Ferrero, A. Lamberti, *Adv. Sustain. Syst.* **2022**, *6*, 2100228.
[21] S. Han, C. Liu, N. Li, S. Zhang, Y. Song, L. Chen, M. Xi, X. Yu, W. Wang, M. Kong, Z. Wang, *CrystEngComm* **2022**, *24*, 1866.
[22] F. Mahmood, H. Zhang, J. Lin, C. Wan, *ACS Omega* **2020**, *5*, 14611.
[23] H. Liu, K.-s. Moon, J. Li, Y. Xie, J. Liu, Z. Sun, L. Lu, Y. Tang, C.-P. Wong, *Nano Energy* **2020**, *77*, 105058.
[24] W. Ma, J. Zhu, Z. Wang, W. Song, G. Cao, *Mater. Today Energy.* **2020**, *18*, 100569.
[25] Z. Peng, R. Ye, J. A. Mann, D. Zakhidov, Y. Li, P. R. Smalley, J. Lin, J. M. Tour, *ACS Nano* **2015**, *9*, 5868.
[26] W. Yang, Y. Liu, Q. Li, J. Wei, X. Li, Y. Zhang, J. Liu, *RSC Adv.* **2020**, *10*, 23953.
[27] K. Y. Kim, H. Choi, C. V. Tran, J. B. In, *J. Power Sources* **2019**, *441*, 227199.
[28] J. B. Lee, J. Jang, H. Zhou, Y. Lee, J. B. In, *Energies* **2020**, *13*, 6567.
[29] S. Greiner, J. Hettig, A. Laws, K. Baumgärtner, J. Bustos, A. Pöppler, C. Adam, M. Nyman, C. Streb, M. Anjass, *Angew. Chem. Int. Ed* **2022**,*61*, 20211454.
[30] M. Anjass, G. A. Lowe, C. Streb, *Angew. Chem. Int. Ed* **2021**, *60*, 7522.
[31] S. Greiner, B. Schwarz, M. Ringenberg, M. Dürr, I. Ivanovic-Burmazovic, M. Fichtner, M. Anjass, C. Streb, *Chem. Sci.* **2020**, *11*, 4450.
[32] F. Li, S. H. Carpenter, R. F. Higgins, M. G. Hitt, W. W. Brennessel, M. G. Ferrier, S. K. Cary, M. P. Shores, M. L. Neidig, S. A. Kozimor, E. M. Matson, *Inorg. Chem.* **2017**, *56*, 7065.
[33] E. Schreiber, N. A. Hartley, W. W. Brennessel, T. R. Cook, J. R. McKone, E. M. Matson, *ACS Appl. Energy Mater.* **2019**, *2*, 8985.
[34] L. Chen, M. J. Turo, M. Gembicky, R. A. Reinicke, A. M. Schimpf, *Angew. Chem.Int. Ed.* **2020**, *59*, 16609.
[35] J.-J. Chen, M. D. Symes, L. Cronin, *Nat. Chem.* **2018**, *10*, 1042.
[36] Q. Zhang, J. Ondus, J. Mills, A. Bahadori, J. Smith, T. Jordan, H. Xu, S. Hwu, *J. Solid State Chem.* **2020**, *287*, 121368.
[37] N. Arya, T. Philipp, S. Greiner, M. Steiner, C. Kranz, M. Anjass, *Angew. Chem.Int. Ed.* **2023**, *62*, 202306170.
[38] H. Lv, Y. V. Geletii, C. Zhao, J. W. Vickers, G. Zhu, Z. Luo, J. Song, T. Lian, D. G. Musaev, C. L. Hill, *Chem. Soc. Rev.* **2012**, *41*, 7572.

[39] N. Hu, J. Du, Y.-Y. Ma, W.-J. Cui, B.-R. Yu, Z.-G. Han, Y.-G. Li, *Appl. Surface Sci.* **2021**, *540*, 148306.
[40] K. Kastner, B. Puscher, C. Streb, *Chem. Commun.* **2013**, *49*, 140.
[41] S. A. Kumar, S. Shiby, A. Sahu, P. Pachori, M. Tanwar, R. Kumar, I. A. Palani, *J. Physics D: Appl. Phys.* **2022**, *56*, 015305.
[42] M. A. Pimenta, G. Dresselhaus, M. S. Dresselhaus, L. G. Cançado, A. Jorio, R. Saito, *Phys. Chem. Chem. Phys.* **2007**, *9*, 1276.
[43] A. C. Ferrari, J. Robertson, *Phys. Rev. B* **2000**, *61*, 14095.
[44] J.-B. Wu, M.-L. Lin, X. Cong, H.-N. Liu, P.-H. Tan, *Chem. Soc. Rev.* **2018**, *47*, 1822.
[45] A. Eckmann, A. Felten, A. Mishchenko, L. Britnell, R. Krupke, K. S. Novoselov, C. Casiraghi, *Nano Lett.* **2012**, *12*, 3925.
[46] D. Sirshendu, T. Braun, F. D. Pammer, J. Choi, S. Fleischmann, M. Fichtner, *Carbon* **2024**, *218*, 118753.
[47] R. Baddour-Hadjean, A. Boudaoud, S. Bach, N. Emery, J.-P. Pereira-Ramos, *Inorg. Chem.* **2014**, *53*, 1764.
[48] X. Dong, C.-Y. Su, W. Zhang, J. Zhao, Q. Ling, W. Huang, P. Chen, L.-J. Li, *Phys. Chem. Chem. Phys.* **2010**, *12*, 2164.
[49] A. Xie, C.-A. Ma, L. Wang, Y. Chu, *Electrochim. Acta* **2007**, *52*, 2945.
[50] S. Boukhalfa, K. Evanoff, G. Yushin, *Energy Environ. Sci.* **2012**, *5*, 6872.
[51] L. Köps, P. Zaccagnini, C. F. Pirri, A. Balducci, *J. Power Sources Adv.* **2022**, *16*, 100098.
[52] J. Wang, J. Polleux, J. Lim, B. Dunn, *J. Phys. Chem. C* **2007**, *111*, 14925.
[53] N. Kumar, M. Singh, A. Kumar, T. Y. Tseng, Y. Sharma, *ACS Appl. Energ. Mater.* **2020**, *3*, 2450.
[54] T. Brezesinski, J. Wang, S. H. Tolbert, B. Dunn, *Nat. Mat.* **2010**, *9*, 146.
[55] A. Sadezky, H. Muckenhuber, H. Grothe, R. Niessner, U. Pöschl, *Carbon* **2005**, *43*, 1731.
[56] C. Schmidt, T. M. Seward, *Chem. Geol.* **2017**, *467*, 64.
[57] J. Hwang, B. Kim, J. Moon, A. Mehmood, H. Y. Ha, *J. Mat. Chem. A* **2018**, *6*, 4695.
[58] B. Soghomon, A. Chrissanthopoulos, R. Fehrmann, *J. Phys. Chem. B* **2002**, *106*, 49.
[59] B. Soghomon, *J. Chem. Soc., Faraday Trans.* **1998**, *94*, 3463.